Research Article

Comparative Study of Adaptive Hamiltonian Control Laws for DC Microgrid Stabilization: An Fuel Cell Boost Converter

Damien Guilbert
Groupe de Recherche en Energie Electrique de Nancy (GREEN), Université de Lorraine, Nancy, France

Babak Nahid-Mobarakeh
Department of Electrical and Computer Engineering, McMaster University, Hamilton, Canada

Serge Pierfederici
Laboratoire d'Energétique et de Mécanique Théorique et Appliquée (LEMTA), Nancy, France

Nicu Bizon
Department of Electronics, Computers and Electrical Engineering, Faculty of Electronics, Communications and Computers, University of Pitesti, Pitesti, Romania

Pongsiri Mungporn
Renewable Energy Research Centre (RERC), Thai-French Innovation Institute, King Mongkut's University of Technology North Bangkok, Bangkok, Thailand

Phatiphat Thounthong*
Renewable Energy Research Centre (RERC), Department of Teacher Training in Electrical Engineering, Faculty of Technical Education, King Mongkut's University of Technology North Bangkok, Bangkok, Thailand

* Corresponding author. E-mail: phatiphat.t@fte.kmutnb.ac.th DOI: 10.14416/j.asep.2021.10.005
Received: 1 March 2021; Revised: 19 May 2021; Accepted: 24 June 2021; Published online: 12 October 2021

Abstract
Future smart grids can be seen as a system of interlinked microgrids, including small-scale local power systems. They consist of main power sources, external loads, and energy storage devices. In these microgrids, the negative incremental impedance behavior of constant power loads (CPLs) is of major concern since it can lead to instability and oscillations. To cope with this issue, this research aims to propose a comparative study of adaptive Hamiltonian control laws, also known as interconnection and damping–assignment–passivity–based controllers (IDA-PBC). These control laws are developed to ensure the stability of the DC output voltage of a boost converter supplied by a proton exchange membrane fuel cell (PEMFC) source. To validate the developed control laws, experiments have been performed on a fit test bench including a real 2.5 kW PEMFC stack (hydrogen is supplied by a reformer engine), a DC-DC step-up circuit, and a real-time controller dSPACE (implementation of the control laws). Moreover, a comparative study has been carried out between the proposed three adaptive Hamiltonian control laws and a classic linear cascaded proportional–integral (PI) control law. The obtained results by simulations through MATLAB/SimulinkTM and experimentally have allowed demonstrating that the third Hamiltonian control law presents the best performances over the other control laws.

Keywords: Constant power load (CPL), Electric vehicle, DC microgrid, Boost converter, Fuel cell (FC), Proportional-Integral controller (PI), Lyapunov function, Port-Hamiltonian (pH), Interconnection and damping-assignment-passivity-based controller (IDA-PBC)

1 Introduction

Over the last decade, eco-green and sustainable energy fuels, such as hydrogen have become a research motivation in the energy domain to cope with global warming and the depletion of fossil fuels. Proton exchange membrane fuel cell (PEMFC) converts hydrogen and oxygen fuels as the reaction raw materials to electricity. It has the advantages of high power density, low-temperature operations (quick start-up), and environmentally friendly during operation (only water and heat are released), which is suitable for DC microgrids (Figure 1) practical into the fields of mobility as well as stationary [1], [2].

The FC stack exhibits a nonlinear voltage-current behavior, and its output voltage v_{FC} is relatively low and unregulated [3], [4]. To boost and regulate this voltage to the DC bus voltage v_C (see Figure 1) and meet the external load constraints, a DC/DC boost converter is commonly interfaced between an FC source and the DC microgrid [3]. The conventional DC/DC boost converter as depicted in Figure 2 is made from a simple circuit including a few components making it easier design and control [5].

Given that the incremental resistance of a constant power load (CPL, such as the tightly closed-loop motor drive) in DC microgrid is negative, supplying this type of load through a power switching circuit can regularly cause large oscillations and instability of the DC bus [6], [7]. In comparison, with constant resistive load (CRL, such as LED lightings), power switching circuits with CPL are unstable in open-loop control [8]. Therefore, a suitable feedback control loop is required to guarantee the stability of the system. In the case of CPLs, the instability of the DC bus connected to the power converters is a challenging issue. Indeed, this issue appeared during the 80s on a regional narrow gauge railway in Switzerland, where railcars were powered by DC motors. To face this issue, DC motors were replaced by induction motors fed by inverters. In that case, slight adjustments on the control structure of the inverter control have enabled solving the problem. The problem of instability of the DC bus is strongly associated with the rated power of the converter system. With the increasing power of the converter system, the efficiency usually increases. Consequently, the inherent damping of the system declines. Besides, the system becomes more prone to this instability. The instability results in a smoothly increasing voltage oscillation, that starts at a certain power level. By properly tuning the power level, it is possible to operate the system continuously with a certain limited voltage oscillation. On the other side, increasing the power level leads immediately to a protective shutdown of the system.

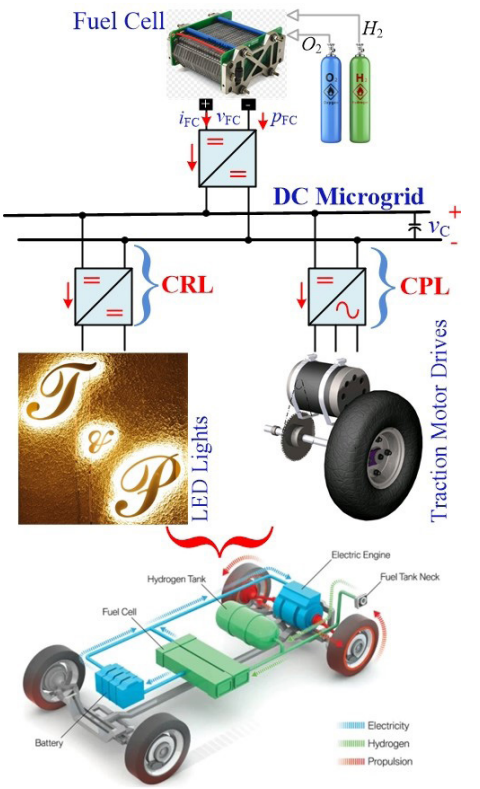

Figure 1: An FC energy source in DC microgrid (stationary or embedded).

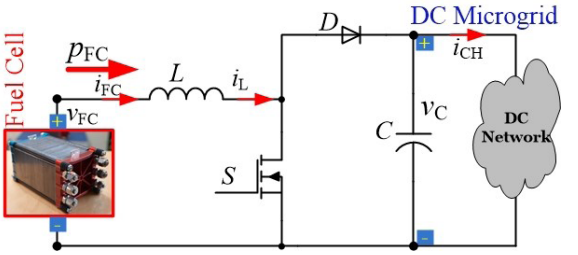

Figure 2: An FC converter based on a classic boost converter topology.

Recently, many stabilization techniques have been studied and implemented for DC microgrids with

CPLs. Originally, Kwasinski and Onwuchekwa [9] and Cespedes *et al.* [10] have proposed the passive-damping techniques by increasing the controlled network damping, which is realized by passive elements like capacitors, inductors, or resistors. Nonetheless, these methods unavoidably increase power losses, reducing consequently network efficiency. In opposite, due to the nonlinear nature of power-switching circuits, nonlinear control methods have been studied and developed as promising replacements to guarantee the stability of DC microgrids with CPLs under large-signal disturbances [11], [12]. It is important to point out that the large load variations of the equilibrium point affected by the varying input voltage make linear approximations insufficient. Hence, to capture the complete dynamics, a nonlinear model is required. Based on the preliminary works developed by Konstantopoulos and Alexandridis [13] and Meshram *et al.* [14], the Hamiltonian–Energy control law or Passivity based controllers (PBCs) or Interconnection and damping-assignment-passivity-based controller (IDA-PBC) have been applied to stabilize the power switching converters. At present, one of the most effective techniques of meeting the CPL stability problem consists of using Port-Control Hamiltonian (PCH) or IDA-PBC [15], [16]. Lately, He *et al.* [17] and Soriano-Rangel *et al.* [18] have proposed an adaptive PBC and provided a comprehensive stability analysis for a buck–boost DC/DC power circuit supplying a CPL. However, the adaptive PBC control laws in [17], [18] have been provided according to a time-scaled model and are tremendously complex to be of practical interest.

The key contribution of this work is to present and compare three proposed Hamiltonian control laws [or (IDA-PBC)] and a classic cascaded proportional integral (PI) control law for an FC step-up converter. The first version of the IDA-PBC for FC boost converter has been presented by Mungporn *et al.* [19], but, it is not an adaptive control. The second version of the Hamiltonian control law for FC boost converter has been introduced by Thounthong *et al.* [20], but, it is not an adaptive control. Recently, the third version of the adaptive Hamiltonian control law for FC boost converter has been provided by Thounthong *et al.* [8]. This paper is a first step to bring new contributions to the large-signal stability analysis of DC microgrids using the passivity control theory.

This paper is structured as follows. A description of the differential equations of the FC boost converter is provided in Section 2. Section 3 presents the linear PI controller and the three adaptive Hamiltonian control laws with stability proofs. In Section 4, the simulations and the realized experimental test bench are detailed, and the obtained results are discussed. Lastly, Section 5 provides a synthesis of the key results and perspectives for future works.

2 Fuel Cell Boost Converter Modelling

The electrical schematic of an FC boost converter supplying the load in a DC microgrid is drawn in Figure 2. S is the power switch and D is the diode. $i_{FC} \in \Re > 0$ is the FC current (= the inductor current i_L), $v_{FC} \in \Re > 0$ is the FC voltage, and $p_{FC} \in \Re > 0$ is the FC power (= $v_{FC} \cdot i_{FC}$). $i_{CH} \in \Re > 0$ is the load current, $v_C \in \Re > 0$ is the DC bus voltage, $p_{CH} \in \Re > 0$ is the load power (= $v_C \cdot i_{CH}$). C is the DC bus output capacitance and L is the input inductance. Considering that the FC boost converter operates in continuous conduction mode (CCM), the well-known differential equations of the classic boost converter is given [20], [21]:

$$\frac{\mathrm{d}i_L}{\mathrm{d}t} = \left(v_{FC} - r_L i_L - v_C + d v_C\right)/L \tag{1}$$

$$\frac{\mathrm{d}v_C}{\mathrm{d}t} = \left(\left(1-d\right) i_L - i_{CH}\right)/C \tag{2}$$

where $d \in [0, 1]$ is the control input duty cycle (*pu.*) of the power switch S that is an important control signal. r_L is the equivalent series resistance (ESR) of an input inductor, L. Note here that r_L corresponds to the fixed loss in the converter module.

3 Control Laws for the FC Boost Converter

The control issue is formulated assuming the following assumptions about the controlled plant presented by Equations (1) and (2). Mathematically, the control input u, the state variables x, and the desired state set-points x_d are defined as [Equations (3)–(5)]:

$$u = d, \tag{3}$$

$$\mathrm{x} = [x_1, x_2]^T, = [i_L, v_C], \tag{4}$$

$$x_d = [x_{1d}, x_{2d}]\mathrm{T}, = [i_{Ld}, v_{Cd}]. \tag{5}$$

Assumption 1: The state (x_1, x_2), the load current i_{CH}, and the FC voltage v_{FC} are measurable.

Assumption 2: The parameters r_L, L, and C are known.

The main control aims to stabilize the important state variable x_2 (= the DC bus voltage v_C) to a desired set-point x_{2d}. Depending on its application in DC microgrid, the value of DC bus voltage v_C may change: x_{2d} = 270 V for the electric aircraft [22]–[24]; 270–540 V for electric cars [25], and 750–1770 V for city tramways and electric trains [26].

3.1 *Cascaded linear PI control law*

For comparison objectives, a summary of the classic cascaded linear PI controllers is expressed as follows [27]–[29]. First, the inner inductor current control allows obtaining the control input u and is expressed as [Equation (6)]:

$$u = K_{Pi}\left(x_{1d} - x_1\right) + K_{Ii}\int_0^t \left(x_{1d} - x_1\right) d\tau \tag{6}$$

where K_{Pi} and K_{Ii} are the tuning proportional and integral gains, respectively. Second, the outer DC bus voltage control is generated through the desired FC power set-point p_{FCd} and is written as [Equation (7)]:

$$p_{FCd} = K_{Pv}\left(x_{2d} - x_2\right) + K_{Iv}\int_0^t \left(x_{2d} - x_2\right) d\tau, \tag{7}$$

with $x_{1d} = p_{FCd}/v_{FC}$,
where K_{Pv} and K_{Iv} are the tuning proportional and integral gains, respectively.

3.2 *Adaptive Hamiltonian control law* I

The well-known port–Controlled Hamiltonian pCH form [30], [31] can be written as follows:

$$\frac{d\mathbf{x}}{dt} = \left[\mathbf{J} - \mathbf{R}\right]\frac{\partial H\left(\mathbf{x}\right)}{\partial \mathbf{x}} + \mathbf{g}\cdot\mathbf{u} + \boldsymbol{\xi}, \tag{8}$$

where $\mathbf{u}$ is the control vector ($\in \Re^m$), $\mathbf{g}$ is the input matrix ($n \times m$), ξ is the external disturbance vector, $\mathbf{x}$ is the state variable vector ($\in \Re^n$), $\mathbf{R} = \mathbf{R}^T \geq 0$ is the damping matrix ($n \times n$), $\mathbf{J} = -\mathbf{J}^T$ is the interconnection matrix ($n \times n$), and $H(\mathbf{x})$ is the Hamiltonian stored energy function (a scalar field) of the controlled plant [32], [33].

According to Equations (3) and (4), the Hamiltonian function in the proposed quadratic equation [34]–[36] is set as [Equations (9) and (10)]:

$$\mathrm{H}\left(x\right) = \frac{1}{2}\mathbf{x}^T\mathbf{Q}_1\,\mathbf{x}, \tag{9}$$

$$\text{where } \mathbf{Q}_1 = \begin{bmatrix} L & 0 \\ 0 & C \end{bmatrix} \tag{10}$$

which can thus be written as [Equation (11)]:

$$\mathrm{H}\left(\mathbf{x}\right) = \frac{1}{2}\left(Lx_1^2 + Cx_2^2\right). \tag{11}$$

As a result, the gradient of a scalar field $H(\mathbf{x})$ with respect to $\mathbf{x}$ can be expressed as:

$$\frac{\partial \mathrm{H}\left(x\right)}{\partial \mathbf{x}} = \begin{bmatrix} Lx_1 & Cx_2 \end{bmatrix}^T. \tag{12}$$

Then, the matrix $\mathbf{J}$, $\mathbf{R}$ and $\mathbf{g}$ and vector ξ can be obtained as:

$$\mathbf{J} = \begin{bmatrix} 0 & \dfrac{-1}{LC} \\ \dfrac{1}{LC} & 0 \end{bmatrix},\ \mathbf{R} = \begin{bmatrix} \dfrac{r_L}{L^2} & 0 \\ 0 & 0 \end{bmatrix},\ \mathbf{g} = \begin{bmatrix} \dfrac{x_2}{L} \\ \dfrac{-x_1}{C} \end{bmatrix}, \text{ and}$$

$$\boldsymbol{\xi} = \begin{bmatrix} \dfrac{v_{FC}}{L} \\ \dfrac{-i_{CH}}{C} \end{bmatrix}. \tag{13}$$

The adaptive Hamiltonian control law I (or the classic IDA-PBC) is written as [37], [38]:

$$\frac{d\mathbf{x}}{dt} = \left[\mathbf{J}_d - \mathbf{R}_d\right]\frac{\partial H_d\left(\mathbf{x}\right)}{\partial \mathbf{x}} \tag{14}$$

It is essential to state the error vector $\mathbf{e} = [e_1, e_2]^T$. It can be written [Equation (15)]:

$$\mathbf{e} = \mathbf{x}_d - \mathbf{x}. \tag{15}$$

Then, the desired Hamiltonian function H_d [Equation (9)] has been chosen as the proposed quadratic function [Equation (16)]:

$$\mathrm{H}_d\left(\mathbf{x}\right) = \frac{1}{2}\mathbf{e}^T\mathbf{Q}_1\,\mathbf{e}, \tag{16}$$

Therefore,

$$\mathrm{H_d}\left(\mathbf{x}\right)=\frac{1}{2}L\cdot\left(x_{1\mathrm{d}}-x_1\right)^2+\frac{1}{2}C\cdot\left(x_{2\mathrm{d}}-x_2\right)^2 \tag{17}$$

Subsequently, the gradient of a scalar field $\mathrm{H_d}(\mathbf{x})$ with respect to $\mathbf{x}$ can be expressed as:

$$\frac{\partial \mathrm{H_d}\left(x\right)}{\partial \mathbf{x}}=\left[L\left(x_1-x_{1\mathrm{d}}\right)\quad C\left(x_2-x_{2\mathrm{d}}\right)\right]^{\mathrm{T}} \tag{18}$$

From the damping control point of view [39], the control interconnection matrix $\mathbf{J}_\mathrm{d}$ and control damping matrix $\mathbf{R}_\mathrm{d}$ are proposed as follows:

$$\mathbf{J}_\mathrm{d}=\begin{bmatrix}0 & -\dfrac{1+K_\mathrm{J}}{LC}\\ \dfrac{1+K_\mathrm{J}}{LC} & 0\end{bmatrix},\ \mathbf{R}_\mathrm{d}=\begin{bmatrix}\dfrac{r_\mathrm{L}+K_\mathrm{R}}{L^2} & 0\\ 0 & 0\end{bmatrix} \tag{19}$$

where $\mathbf{J}_\mathrm{d}=-\mathbf{J}_\mathrm{d}^{\mathrm{T}}$, $\mathbf{R}_\mathrm{d}=\mathbf{R}_\mathrm{d}^{\mathrm{T}}\geq 0$, and $K_\mathrm{R}\in\Re\geq 0$ is the tuning controller used to damp the transient oscillations. $K_\mathrm{J}\in\Re$ is the real-time adaptive gain. Then, combining Equations (12), Equation (13) into Equations (8) and (18), Equation (19) into Equation (14), the matching equation of the control law I can be deduced as Equation (20) (shown at the bottom of the page).

Finally, by solving the Equation (20), there are two equations and two unknown variables u, K_J to be solved with one tuning controller K_R. So, the unique solution of the control law I can be obtained as [Equations (21) and (22)]:

$$\begin{aligned}K_\mathrm{J}=&-(i_{\mathrm{CH}}x_2-v_{\mathrm{FC}}x_1+x_1x_{2\mathrm{d}}-x_2x_{1\mathrm{d}}-K_\mathrm{R}{x_1}^2+\ldots\\&K_\mathrm{R}x_1x_{1\mathrm{d}}+r_\mathrm{L}x_1x_{1\mathrm{d}})/(x_1x_{2\mathrm{d}}-x_2x_{1\mathrm{d}})\end{aligned} \tag{21}$$

$$u=\frac{x_{2\mathrm{d}}-v_{\mathrm{FC}}+r_\mathrm{L}x_{1\mathrm{d}}+K_\mathrm{R}e_1+K_\mathrm{J}e_2}{x_2} \tag{22}$$

Then, to generate the desired state $x_{1\mathrm{d}}$ (the FC current set-point), the load power estimation may be written as:

$$p_{\mathrm{CH}}=v_\mathrm{C}i_{\mathrm{CH}}=x_2i_{\mathrm{CH}} \tag{23}$$

At equilibrium point, one may simplify $x_2=x_{2\mathrm{d}}$ as:

$$p_{\mathrm{CH}}=x_{2\mathrm{d}}i_{\mathrm{CH}} \tag{24}$$

By setting $\mathrm{d}x/\mathrm{d}t=0$ and $\boldsymbol{x}=\boldsymbol{x}_\mathrm{d}$ of Equations (1) and (2). Then, the desired input power fix-point p_{FCd} can be written as:

$$p_{\mathrm{FCd}}=2p_{\mathrm{FCMax}}\left(1-\sqrt{1-\frac{p_{\mathrm{CH}}}{p_{\mathrm{FCMax}}}}\right), \tag{25}$$

$$\text{with } p_{\mathrm{FCMax}}=\frac{{v_{\mathrm{FC}}}^2}{4r_L}. \tag{26}$$

Then,

$$x_{1\mathrm{d}}=\frac{p_{\mathrm{FCd}}}{v_{\mathrm{FC}}}. \tag{27}$$

Stability proof: Adaptive Control Law I

According to Equation (17), $\mathrm{H_d}(\mathbf{x})$ is a positive-definite function; as a result, it can be proposed as the Lyapunov candidate function V [40], [41].

$$V=\mathrm{H_d}(\mathbf{x})>0. \tag{28}$$

Then, the derivative of V can be obtained as [Equation (29)]

$$\frac{\mathrm{d}V}{\mathrm{d}t}=\frac{\mathrm{d}H_\mathrm{d}\left(\mathbf{x}\right)}{\mathrm{d}t}=\left(\frac{\partial\mathbf{H}_\mathrm{d}\left(\mathbf{x}\right)}{\partial\mathbf{x}}\right)^{\mathrm{T}}\frac{\mathrm{d}\mathbf{x}}{\mathrm{d}t} \tag{29}$$

$$\frac{\mathrm{d}V}{\mathrm{d}t}=-\left[\left(\frac{\partial\mathbf{H}_\mathrm{d}\left(\mathbf{x}\right)}{\partial\mathbf{x}}\right)^{\mathrm{T}}\mathbf{R}_\mathrm{d}\frac{\partial\mathbf{H}_\mathrm{d}\left(\mathbf{x}\right)}{\partial\mathbf{x}}\right]_{K_\mathrm{R}>0}<0. \tag{30}$$

Combining Equations (28) and (30) gives $V>0$ and $\mathrm{d}V/\mathrm{d}t<0$; thus, the adaptive control law I can exhibit large-signal asymptotic stability, completing the proof.

3.3 *Adaptive Hamiltonian control law* II

The proposed control law II is similar to the control law I by using the same forms of Equations (8) and (14).

$$\overbrace{\begin{bmatrix}-\dfrac{r_\mathrm{L}+K_\mathrm{R}}{L^2} & -\dfrac{1+K_\mathrm{J}}{LC}\\ \dfrac{1+K_\mathrm{J}}{LC} & 0\end{bmatrix}}^{\mathbf{J}_\mathrm{d}-\mathbf{R}_\mathrm{d}}\overbrace{\begin{bmatrix}L\left(x_1-x_{1\mathrm{d}}\right)\\ C\left(x_2-x_{2\mathrm{d}}\right)\end{bmatrix}}^{\frac{\partial H_\mathrm{d}(\mathbf{x})}{\partial\mathbf{x}}}=\overbrace{\begin{bmatrix}-\dfrac{r_L}{L^2} & \dfrac{-1}{LC}\\ \dfrac{1}{LC} & 0\end{bmatrix}}^{\mathbf{J}-\mathbf{R}}\overbrace{\begin{bmatrix}Lx_1\\ Cx_2\end{bmatrix}}^{\frac{\partial H(\mathbf{x})}{\partial\mathbf{x}}}+\overbrace{\begin{bmatrix}\dfrac{x_2}{L}\\ \dfrac{-x_1}{C}\end{bmatrix}}^{\mathbf{g}}\cdot\overbrace{u}^{\mathbf{u}}+\overbrace{\begin{bmatrix}\dfrac{v_{\mathrm{FC}}}{L}\\ -i_{\mathrm{CH}}\\ C\end{bmatrix}}^{\xi} \tag{20}$$

The main weak point of the control law I (the classic IDA-PBC) is that it does not allow guaranteeing $e_2 \neq 0$ ($x_{2d} \neq x_2$) because of model errors, parasitic elements, uncertainties, and noises. Accordingly, the standard integral term is included to cope with this important issue and to improve the controlled system. A new variable λ is defined as:

$$\lambda = K_I \int_o^\tau \left(v_{Cd} - v_C\right) dt, \tag{31}$$

where K_I is the tuning integral gain. Then, the extended converter model in 3-dimensions with the supplementary integrator term Equation (31) can be obtained in p_{CH} form with the new extended state variables **x** [Equation (32)]:

$$\mathbf{x} = \begin{bmatrix} x_1 & x_2 & x_3 \end{bmatrix}^T = \begin{bmatrix} i_L & v_C & \lambda \end{bmatrix}^T. \tag{32}$$

The extended Hamiltonian function in the proposed quadratic equation is set as [42], [43] [Equations (33) and (34)]:

$$H(x) = \frac{1}{2} \mathbf{x}^T \mathbf{Q}_{II}\, \mathbf{x}, \tag{33}$$

$$\text{where } \mathbf{Q}_{II} = \begin{bmatrix} L & 0 & 0 \\ 0 & C & 0 \\ 0 & 0 & \dfrac{1}{K_I} \end{bmatrix} \tag{34}$$

which can therefore be written as [Equation (35)]:

$$H(\mathbf{x}) = \frac{1}{2}\left(Lx_1^2 + Cx_2^2 + K_I^{-1} x_3^2\right). \tag{35}$$

Therefore, the gradient of a scalar field $H(\mathbf{x})$ with respect to **x** can be obtained as:

$$\frac{\partial H_I(x)}{\partial \mathbf{x}} = \begin{bmatrix} Lx_1 & Cx_2 & K_I^{-1} x_3 \end{bmatrix}^T. \tag{36}$$

According to Equations (1), (2) and (8), the extended matrix **J**–**R** and **g** and vector ξ can be given as:

$$\mathbf{J} - \mathbf{R} = \begin{bmatrix} -\dfrac{r_L}{L^2} & \dfrac{-1}{LC} & 0 \\ \dfrac{1}{LC} & 0 & 0 \\ 0 & \dfrac{-K_I}{C} & 0 \end{bmatrix}, \mathbf{g} = \begin{bmatrix} \dfrac{x_2}{L} \\ \dfrac{-x_1}{C} \\ 0 \end{bmatrix} \text{ and}$$

$$\boldsymbol{\xi} = \begin{bmatrix} \dfrac{v_{FC}}{L} \\ \dfrac{-i_{CH}}{C} \\ K_I x_{2d} \end{bmatrix}. \tag{37}$$

Afterward, the new error vector **e** is set as [Equation (38)]:

$$\mathbf{e} = \mathbf{x}_d - \mathbf{x} = \begin{bmatrix} e_1 & e_2 & e_3 \end{bmatrix}^T. \tag{38}$$

According to Equation (33), the desired Hamiltonian function $H_d(x)$ is set as:

$$H_d(x) = \frac{1}{2} \mathbf{e}^T \mathbf{Q}_{II}\, \mathbf{e} \tag{39}$$

Then,

$$H_d(\mathbf{x}) = \frac{1}{2} L \cdot \left(x_{1d} - x_1\right)^2 + \frac{1}{2} C \cdot \left(x_{2d} - x_2\right)^2 + \ldots \frac{1}{2} K_I^{-1} \cdot \left(x_{3d} - x_3\right)^2. \tag{40}$$

The gradient of a scalar field $H_d(\mathbf{x})$ with respect to **x** can be expressed as:

$$\frac{\partial H_d(x)}{\partial \mathbf{x}} = \begin{bmatrix} L\left(x_1 - x_{1d}\right) & C\left(x_2 - x_{2d}\right) & K_I^{-1} x_3 \end{bmatrix}^T \tag{41}$$

with $x_{3d} = 0$.

Next, the control interconnection matrix $\mathbf{J}_d$ and control damping matrix $\mathbf{R}_d$ are proposed as follows:

$$\mathbf{J}_d = \begin{bmatrix} 0 & \dfrac{-\left(1+K_J\right)}{LC} & 0 \\ \dfrac{\left(1+K_J\right)}{LC} & 0 & \dfrac{K_I}{C} \\ 0 & \dfrac{-K_I}{C} & 0 \end{bmatrix}, \text{ and}$$

$$\mathbf{R}_d = \begin{bmatrix} \dfrac{\left(r_L + K_R\right)}{L^2} & 0 & 0 \\ 0 & 0 & 0 \\ 0 & 0 & 0 \end{bmatrix} \tag{42}$$

$$\overbrace{\begin{bmatrix} -\frac{(r_L+K_R)}{L^2} & -\frac{(1+K_J)}{LC} & 0 \\ \frac{(1+K_J)}{LC} & 0 & \frac{K_I}{C} \\ 0 & \frac{-K_I}{C} & 0 \end{bmatrix}}^{\mathbf{J_d}-\mathbf{R_d}} \overbrace{\begin{bmatrix} L(x_1-x_{1d}) \\ C(x_2-x_{2d}) \\ K_I^{-1}x_3 \end{bmatrix}}^{\frac{\partial H_d(\mathbf{x})}{\partial \mathbf{x}}} = \overbrace{\begin{bmatrix} -\frac{r_L}{L^2} & \frac{-1}{LC} & 0 \\ \frac{1}{LC} & 0 & 0 \\ 0 & \frac{-K_I}{C} & 0 \end{bmatrix}}^{\mathbf{J}-\mathbf{R}} \overbrace{\begin{bmatrix} Lx_1 \\ Cx_2 \\ K_I^{-1}x_3 \end{bmatrix}}^{\frac{\partial H(\mathbf{x})}{\partial \mathbf{x}}} + \overbrace{\begin{bmatrix} \frac{x_2}{L} \\ \frac{-x_1}{C} \\ 0 \end{bmatrix}}^{\mathbf{g}} \cdot \overbrace{u}^{\mathbf{u}} + \overbrace{\begin{bmatrix} \frac{v_{FC}}{L} \\ \frac{-i_{CH}}{C} \\ K_I x_{2d} \end{bmatrix}}^{\xi} \tag{43}$$

where $\mathbf{J}_d = -\mathbf{J}_d^T$, $\mathbf{R}_d = \mathbf{R}_d^T \geq 0$, and $K_R \in \Re \geq 0$ is the tuning controller used to damp the transient oscillations. $K_J \in \Re$ is the real-time adaptive gain. Then, combining Equation (36), Equation (37) into Equation (8) and (41), Equation (42) into (14), the matching equation of the control law II can be deduced as Equation (43) (shown at the top of the page).

Finally, by solving the Equation (43), the last bottom equation is equal to zero, so there are two equations and two unknown variables u, K_J to be solved with two setting gains K_R and K_I. As a result, the unique solution of the control law II can be obtained as [Equation (44)]:

$$\begin{aligned} K_J = & -(i_{CH}x_2 - v_{FC}x_1 + x_1x_{2d} - x_2x_{1d} - K_R x_1^2 + \ldots \\ & + x_2x_3 + K_R x_1x_{1d} + r_L x_1x_{1d})/(x_1x_{2d} - x_2x_{1d}) \end{aligned} \tag{44}$$

$$u = \frac{x_{2d} - v_{FC} + r_L x_{1d} + K_R e_1 + K_J e_2}{x_2}$$

Finally, according to Equations (23), (24) and (31), the load power estimation may be deduced as [Equation (45)]:

$$p_{CH} = x_{2d}i_{CH} + x_{2d}x_3 \tag{45}$$

Next, to estimate x_{1d}, the same Equations (25)–(27) can be used.

Stability proof: Adaptive Control Law II

According to Equation (40), $H_d(\mathbf{x})$ is a positive-definite function; and it can be proposed as the Lyapunov candidate function V.

$$V = H_d(\mathbf{x}) > 0. \tag{46}$$

Then, the derivative of V can be obtained as:

$$\frac{dV}{dt} = \frac{dH_d(\mathbf{x})}{dt} = \left(\frac{\partial \mathbf{H}_d(\mathbf{x})}{\partial \mathbf{x}}\right)^T \frac{d\mathbf{x}}{dt} \tag{47}$$

$$\frac{dV}{dt} = -\left[\left(\frac{\partial \mathbf{H}_d(\mathbf{x})}{\partial \mathbf{x}}\right)^T \mathbf{R}_d \frac{\partial \mathbf{H}_d(\mathbf{x})}{\partial \mathbf{x}}\right]_{K_R>0} < 0. \tag{48}$$

Combining Equation (46) and (48) gives $V > 0$ and $dV/dt < 0$; hence, the adaptive control law II can exhibit large-signal asymptotic stability, completing the proof.

3.4 *Adaptive Hamiltonian control law* III

In the control laws I and II, the desired set-point $\boldsymbol{x}_d$ is related to the external disturbance ξ (e.g., the FC input voltage v_{FC}, and load current i_{CH}). In a single DC/DC converter, $\boldsymbol{x}_d$ is considered constant or is supposed to change very slowly. However, due to the cascade structure in the DC microgrid, the external input of each subsystem is related to its neighboring system, so it cannot be considered a constant value; it means $\boldsymbol{x}_d = f(\xi)$. According to the stability proof of the control law I and II, the derivative of Lyapunov candidate function V with respect to time results in [Equation (49)]:

$$\frac{dV}{dt} = \frac{dH_d(\mathbf{x})}{dt} \tag{49}$$

$$\frac{dV}{dt} = \overbrace{\left(\frac{\partial H_d(\mathbf{x})}{\partial \mathbf{x}}\right)^T \frac{d\mathbf{x}}{dt}}^{<0} + \left(\frac{\partial H_d(\mathbf{x})}{\partial \mathbf{x}_d}\right)^T \frac{d\mathbf{x}_d}{dt} \tag{50}$$

It can be perceived that the proof of stability written in Equation (50) cannot longer applied for $dV/dt < 0$, and the cascaded controlled network in DC microgrids requires a new viewpoint for control and analysis. To overcome this drawback in the control law Equation (14), the adaptive Hamiltonian–energy control law III is studied as:

$$\frac{d\mathbf{x}}{dt} = [\mathbf{J}_d - \mathbf{R}_d]\frac{\partial H_d(\mathbf{x})}{\partial \mathbf{x}} + \frac{d\mathbf{x}_d}{dt} \tag{51}$$

$$\overbrace{\begin{bmatrix} -\frac{(r_L+K_R)}{L^2} & \frac{-(1+K_J)}{LC} & 0 \\ \frac{(1+K_J)}{LC} & 0 & \frac{K_I}{C} \\ 0 & \frac{-K_I}{C} & 0 \end{bmatrix}}^{\mathbf{J}_d-\mathbf{R}_d} \overbrace{\begin{bmatrix} L(x_1-x_{1d}) \\ C(x_2-x_{2d}) \\ K_I^{-1}x_3 \end{bmatrix}}^{\frac{\partial H_d(\mathbf{x})}{\partial \mathbf{x}}} + \overbrace{\begin{bmatrix} \dot{x}_{1d} \\ \dot{x}_{2d} \\ \dot{x}_{3d} \end{bmatrix}}^{\dot{\mathbf{x}}_d} = \overbrace{\begin{bmatrix} -\frac{r_L}{L^2} & \frac{-1}{LC} & 0 \\ \frac{1}{LC} & 0 & 0 \\ 0 & \frac{-K_I}{C} & 0 \end{bmatrix}}^{\mathbf{J}-\mathbf{R}} \overbrace{\begin{bmatrix} Lx_1 \\ Cx_2 \\ K_I^{-1}x_3 \end{bmatrix}}^{\frac{\partial H(\mathbf{x})}{\partial \mathbf{x}}} + \overbrace{\begin{bmatrix} \frac{x_2}{L} \\ \frac{-x_1}{C} \\ 0 \end{bmatrix}}^{\mathbf{g}} \cdot \underset{\sim}{u} + \overbrace{\begin{bmatrix} \frac{v_{FC}}{L} \\ \frac{-i_{CH}}{C} \\ K_I x_{2d} \end{bmatrix}}^{\xi} \quad (52)$$

Control law III consists of modifying the control structure of control law II with an additional derivative term of the desired state vector $\boldsymbol{x}_d$. So, Equation (42) may write in form of Equation (51) to be Equation (52) (shown at the top of the page).

Therefore, the unique solution of the control law III can be obtained as [Equations (53) and (54)]:

$$K_J = -(i_{CH}x_2 - v_{FC}x_1 + x_1x_{2d} - x_2x_{1d} - K_R x_1^2 + \ldots + x_2x_3 + K_R x_1x_{1d} + r_L x_1x_{1d} + Lx_1\frac{dx_{1d}}{dt} + \ldots + Cx_2\frac{dx_{2d}}{dt})/(x_1x_{2d} - x_2x_{1d}) \quad (53)$$

$$u = \frac{x_{2d} - v_{FC} + r_L x_{1d} + K_R e_1 + K_J e_2 + L\frac{dx_{1d}}{dt}}{x_2} \quad (54)$$

Note that according to Equation (41) $x_{3d} = 0$ then $dx_{3d}/dt = 0$.

Stability proof: Adaptive Control Law III

$H_d(\mathbf{x})$ [Equations (39) and (40)] is a positive-definite function and $\mathbf{e} = \mathbf{x}_d - \mathbf{x}$; then, $H_d(\mathbf{e})$ may be written. Consequently, $H_d(\mathbf{e})$ can be set as the Lyapunov candidate function V, which can be written as [Equation (55)]:

$$V(\mathbf{e}) = H_d(\mathbf{e}) > 0. \quad (55)$$

According to Equation (40), the gradient of a scalar field $H_d(\mathbf{x})$ can be extended as follows:

$$\frac{\partial H_d(x)}{\partial \mathbf{x}} = -\mathbf{Q}_{II}\mathbf{e}. \quad (56)$$

Next, the derivative of the error vector $\mathbf{e}$ can be expressed as [Equation (57)]:

$$\frac{d\mathbf{e}}{dt} = \frac{d\mathbf{x}_d}{dt} - \frac{d\mathbf{x}}{dt}. \quad (57)$$

Substituting Equations (51) and (56) into Equation (57), the following derivative can be obtained [Equation (58)]:

$$\frac{d\mathbf{e}}{dt} = [\mathbf{J}_d - \mathbf{R}_d][-\mathbf{Q}_{II}\mathbf{e}]. \quad (58)$$

As a result, the derivative of $V(\mathbf{e}, t)$ can be presented as [Equation (59)]:

$$\frac{dV(\mathbf{e},t)}{dt} = [-\mathbf{Q}_{II}\mathbf{e}]^T[\mathbf{J}_d - \mathbf{R}_d][-\mathbf{Q}_{II}\mathbf{e}] \quad (59)$$

$\mathbf{J}_d$ is an anti-symmetric matrix ($\mathbf{J}_d = -\mathbf{J}_d^T$), then $[-\mathbf{Q}_{II}\mathbf{e}]^T\mathbf{J}_d[-\mathbf{Q}_{II}\mathbf{e}] \equiv 0$ and $\mathbf{R}_d$ is a positive-definite matrix ($\mathbf{R}_d = \mathbf{R}_d^T \geq 0$). Therefore, the derivative of $V(\mathbf{e})$ can be expressed as [Equation (60)]:

$$\frac{dV(\mathbf{e},t)}{dt} = -[-\mathbf{Q}_{II}\mathbf{e}]^T\mathbf{R}_d[-\mathbf{Q}_{II}\mathbf{e}] < 0. \quad (60)$$

Combining the results $V(\mathbf{e}, t) > 0$ and $dV(\mathbf{e}, t)/dt < 0$, the proposed control law features asymptotical stability at the operating fixed point, thus completing the proof.

3.5 *Control conclusion*

The linear cascaded PI control law, adaptive Hamiltonian control law I, II, and III are summarized and sketched in the simple block diagrams in Figure 3. It is clear that the linear PI control law is a cascade structure, but for the proposed adaptive control law I, II, and III are in a single loop control. For the adaptive control law I, the generation d (= u) depends only on a constant proportional (P) gain K_R and an adaptive gain K_J; one may name the adaptive Hamiltonian P controller. For the adaptive control law II, the generation d (= u) depends on a constant gain K_R and an adaptive gain K_J; but the generation of x_{1d} and K_J are in function of the integral (I) term x_3 Equation (31); one may name the adaptive Hamiltonian PI controller. For the adaptive control law III, it is the extended control law II with the

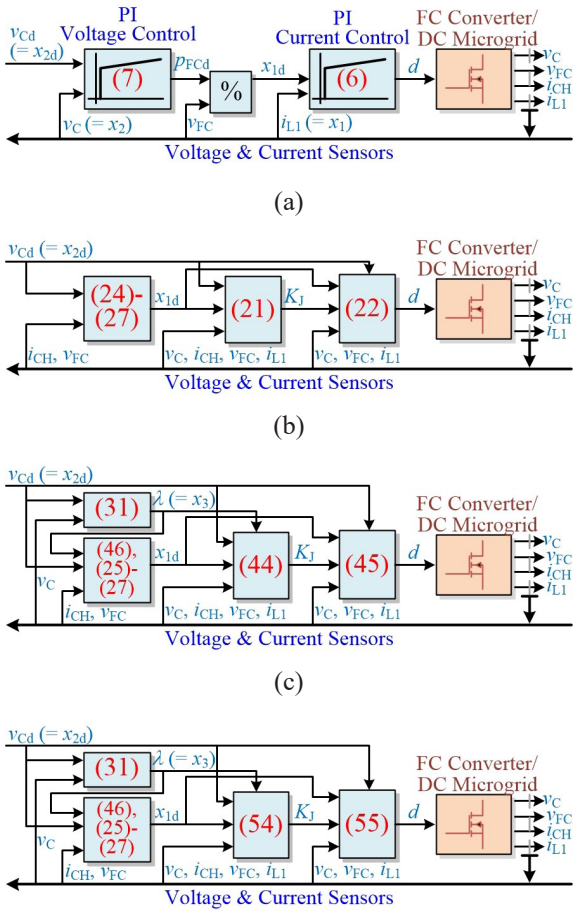

Figure 3: Block diagrams of control laws for an FC step-up converter:
(a) Linear cascaded PI control law,
(b) Adaptive Hamiltonian-energy control law I,
(c) Adaptive Hamiltonian-energy control law II,
(d) Adaptive Hamiltonian-energy control law III.

added derivative (D) term; one may name the adaptive Hamiltonian PID controller.

4 Performance Validation

Firstly, simulations have been performed to validate the effectiveness of the proposed control techniques in terms of the parameter uncertainties by utilizing a switching model of the FC step-up circuit in Matlab/Simulink™. The converter parameters tested in the simulation are summarized in Table A1. For the linear cascaded PI controller, the controller tunings have been designed so that the inner-current loop bandwidth is much larger than that of the outer voltage control loop; there are $K_{Pi} = 0.01\ A^{-1}$, $K_{Ii} = 400\ A \cdot s^{-1}$, $K_{Pv} = 40\ W \cdot V^{-1}$ and $K_{Iv} = 50{,}000\ W \cdot V \cdot s^{-1}$. For the adaptive Hamiltonian control laws, K_R (= 0.5 Ω) is set at five times of r_L (= 0.1 Ω); K_I (= 50) is set at << the converter resonant frequency $1/sqrt(LC)$. Figures 4–6 plot the dynamic characteristics of the DC bus voltage stabilization with CRL and CPL disturbances using a linear PI controller and the studied adaptive controllers. They show the DC bus voltage v_C, the input FC power p_{FC}, and duty cycle d. For the first scenario CRL (Figure 4), the external load resistor r_{CH} is stepped from 9.6 to 7.2 Ω at t = 2.5 ms; this indicates that the load power equilibrium point changes from 1.5 to 2 kW, revealing that using the proposed adaptive Hamiltonian control law III, the DC bus voltage is regulated faster with a lower voltage deviation and lower settling time, leading to stronger robustness against CRLs. There are static errors in the DC bus voltage by using the control law I. Next, for the second scenario CPL (Figure 5), the external load power is stepped from 1.5 to 2 kW at t = 10 ms. There are also static errors in the DC bus voltage by using the control law I. The performance of the cascaded PI algorithm is lower than that of the proposed adaptive controllers and the transient behavior of the PI method exhibits critical performance, with a very large overshoot and oscillations. The proposed control law III shows the best DC bus voltage stabilization; the DC bus voltage undershoots when the power increase is 2.50% (3 V) and the associated settling time is around 5 ms. More importantly, for the third scenario CPL (Figure 6), it shows only the PI control law, adaptive control law II and III. The external load power is stepped from 2.4 to 3 kW at t = 5 ms. The cascaded PI algorithm exhibits low performance, such as instability. On the other side, the proposed control law III exhibits the best DC bus voltage stabilization; the DC bus voltage undershoots when the power increase is 8.33% (10 V) and the associated settling time is around 20 ms. It is clear that the adaptive Hamiltonian control law III presents the best performance; then the following simulations and experimental results show only the results with the adaptive Hamiltonian control law III. For the fourth scenario CPL as displayed in Figure 7 and given that the adaptive control law III is located in the plane, it is the potential to achieve a comprehensive

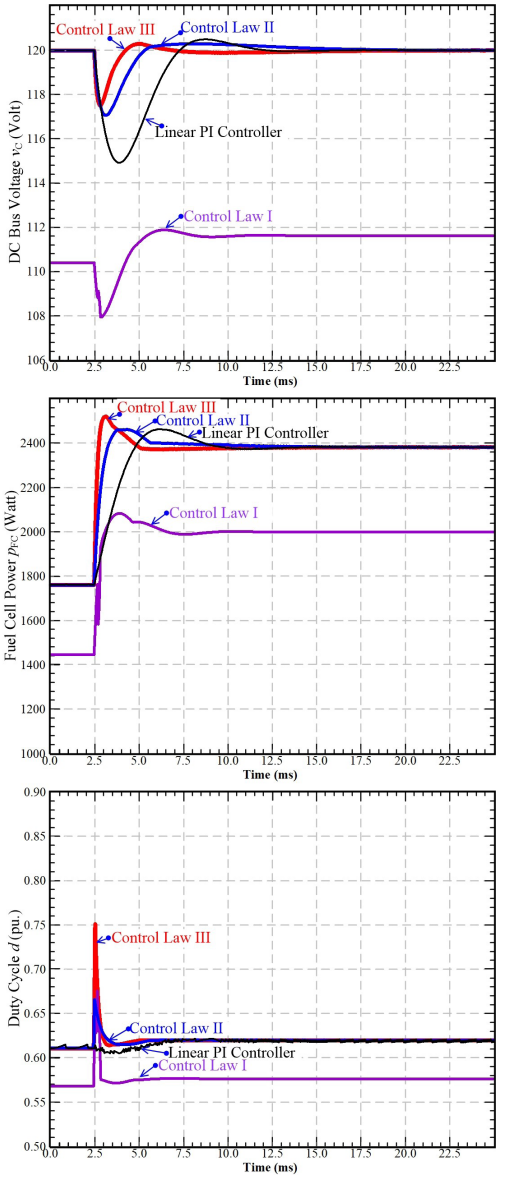

Figure 4: Simulation results: Transient performance comparisons of the controlled FC converter under CRL step changes of r_{CH} from 9.6 to 7.2 Ω.

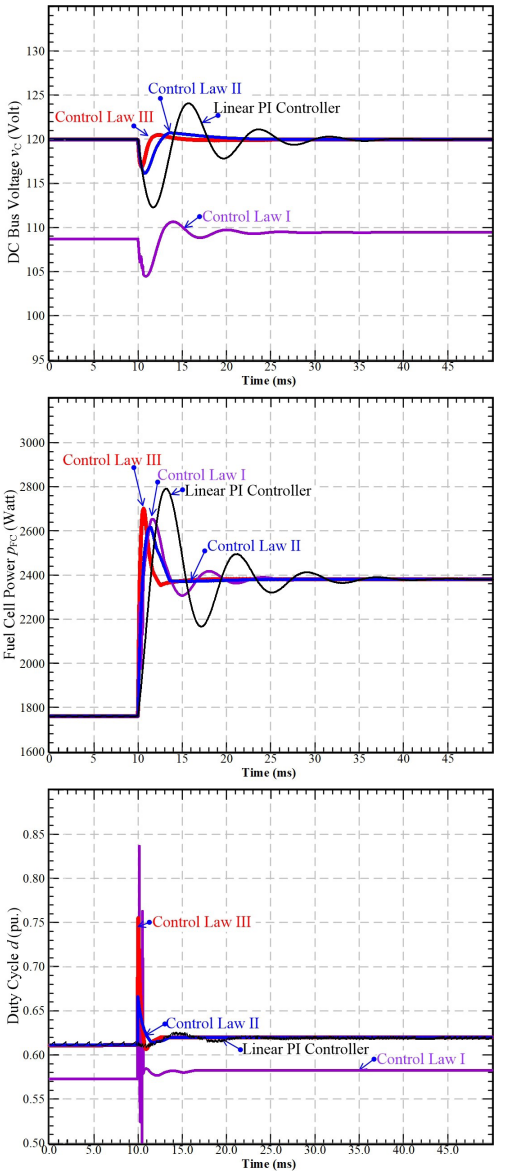

Figure 5: Simulation results: Transient performance comparisons of the controlled FC converter under CPL step changes of p_{CH} from 1.5 to 2 kW.

picture of the performance of the controller by drawing their phase plot. These plots are obtained with a wide range of initial conditions (*) with some trajectories. The final equilibrium point (∇) is defined as $\mathbf{x}_d = (x_{1d}, x_{2d}) = (51.23\ \text{A}, 120\ \text{V})$ so that the load power CPL equals 2 kW. It can be seen that the system converges to the desired equilibrium point (∇).

Next, Figures 8–12 display the simulation and experimental results (the description of the experimental test bench can be seen in Appendix) obtained for the converter regulator with the proposed control law III by setting the controller gains $K_R = 0.5\ \Omega$ and $K_I = 15$. CH1 – CH7 show the DC bus voltage v_C, FC voltage v_{FC}, load power p_{CH}, FC power p_{FC}, FC current i_{FC} (= i_L),

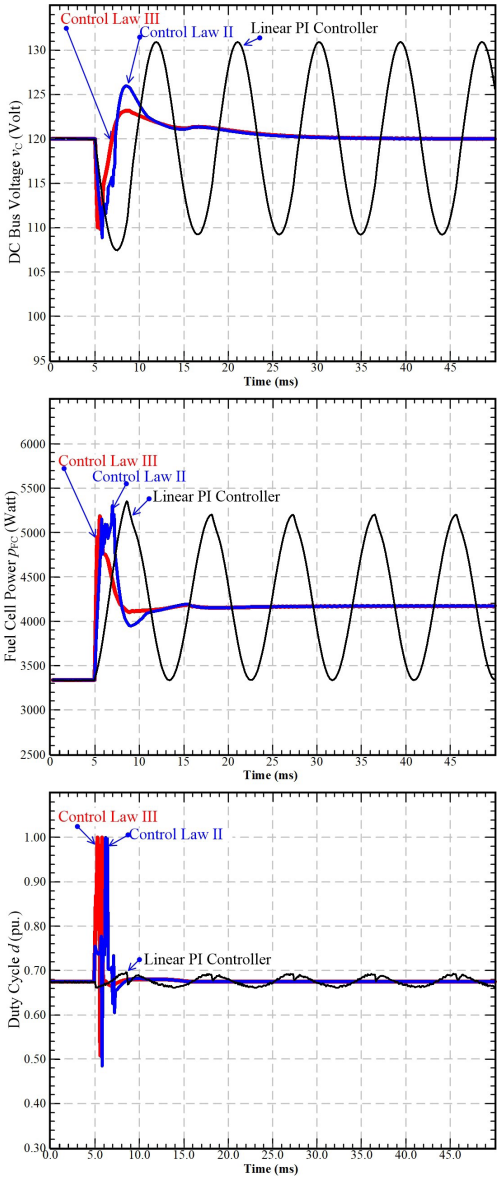

Figure 6: Simulation results: Transient performance comparisons of the controlled FC converter under CPL step changes of p_{CH} from 2.4 to 3 kW.

integral output variable x_3 [= λ, Equation (31)], and adaptive gain K_J, respectively.

For the fifth and sixth scenario CPLs, the equilibrium-point data with CPLs in Figures 8 and 9 illustrate the switching characteristics of the power converter at $v_{Cd} = v_C = 120$ V and $p_{CH} = 800$ W (CCM) and 70 W (DCM), respectively. As a result of the integral action

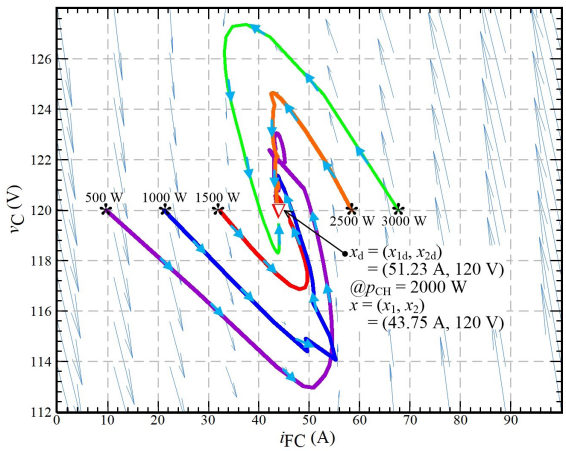

Figure 7: Simulation results: Phase plots of the controlled FC converter with the control law III for different initial conditions CPLs.

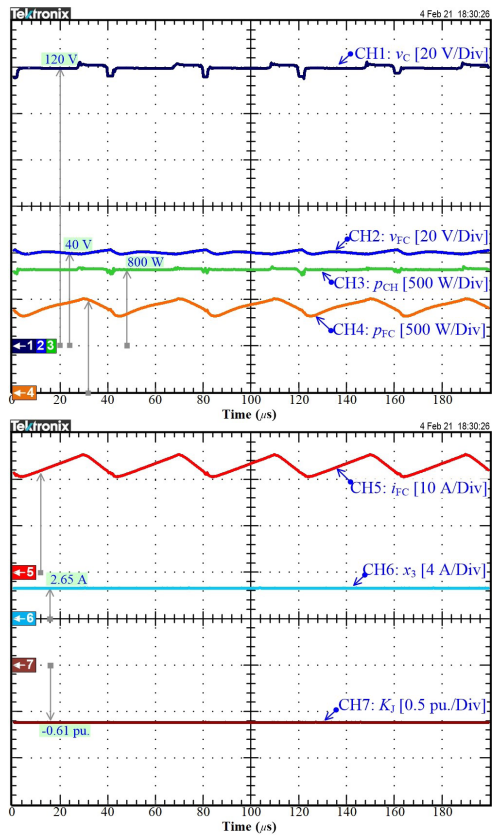

Figure 8: Experimental results: Switching characteristics of the controlled FC converter (at CCM) with the control law III under CPL of $p_{CH} = 800$ W.

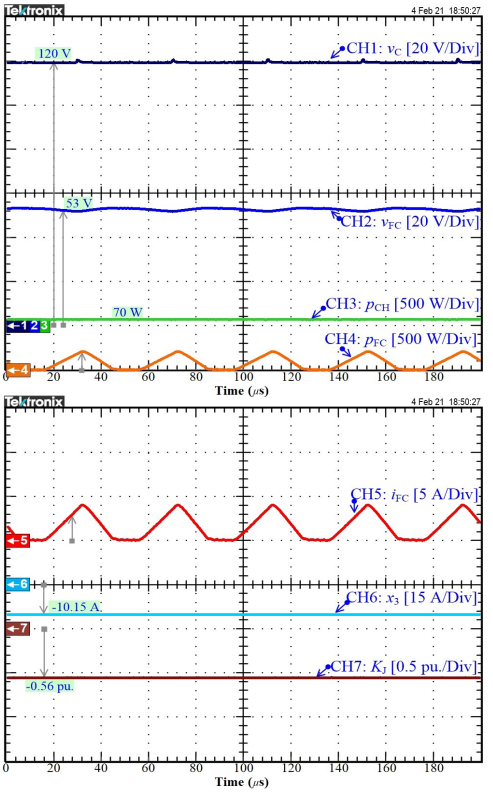

Figure 9: Experimental results: Switching characteristics of the controlled FC converter (at DCM) with the control law III under CPL of p_{CH} = 70 W.

Equation (31) with x_3 of approximately 2.63 A (for load 800 W) and –10.15 A (for load 70 W), it can be seen that f_s = 25 kHz and the converter is well regulated under CCM and DCM.

For the seventh scenario CPL, Figure 10 displays the simulation and experimental results obtained for the converter regulator with the proposed control law III. The CPL changes from 250 to 770 W at t = 10 ms. In Figure 10(b), the DC bus voltage undershoots when increasing the power is 3.33% (4 V) and the associated settling time is 2.5 ms. It can be noted that the adaptive gain K_J is updated depending on the equilibrium point to find an optimum value and the small different waveforms at a time scale of 5 ms/div can be seen between simulation and test bench results because of the modeling errors (the FC model and converter model). However, a good agreement can be observed between the simulation and experimental results in the laboratory test bench.

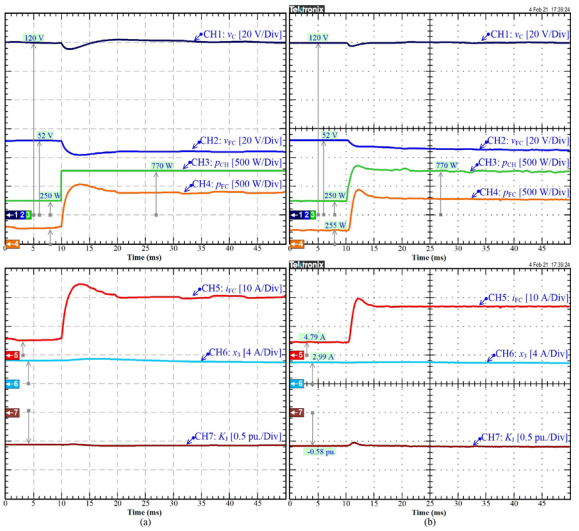

Figure 10: Transient performance of the controlled FC converter with the control law III under CPL step changes of p_{CH} from 250 to 770 W: (a) Simulation results, (b) Experimental results.

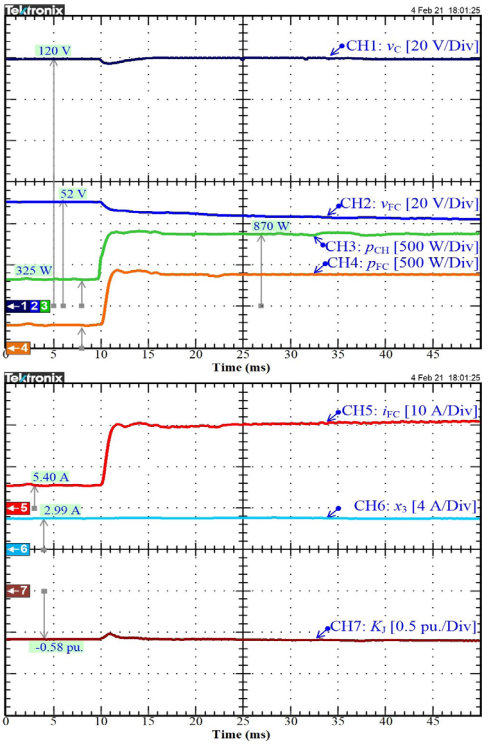

Figure 11: Experimental results: Transient performance of the controlled FC converter with the control law III under CRL step changes of rCH from 44.31 to 16.55 Ω.

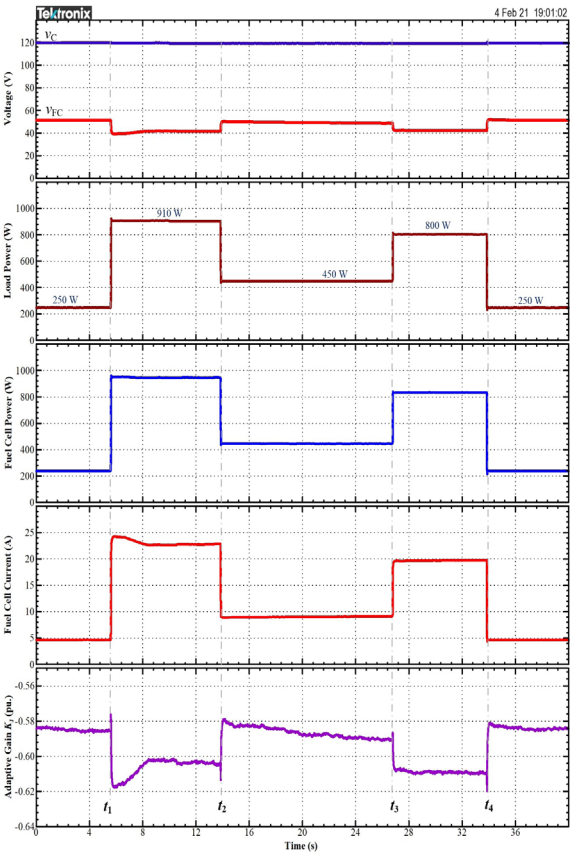

Figure 12: Experimental results: Transient performance of the controlled FC converter with the adaptive Hamiltonian control law III under CPL step changes: Load cycles.

For the eighth scenario CRL, Figure 11 displays the experimental results obtained for the external load resistor rCH step changed from 44.31 to 16.55 Ω at t = 10 ms; this indicates that the equilibrium point changes from 325 to 870 W, showing that using the proposed Hamiltonian controller III, the DC bus voltage is well regulated, leading to enhanced robustness against CRLs.

For the final scenario CPLs, Figure 12 displays the experimental results obtained for CPLs step changed from 250 W to 910 W at t_1; from 910 W to 450 W at t_2; from 450 W to 800 W at t_3; and from 800 W to 250 W at t_4; demonstrating that using the proposed Hamiltonian controller III, the DC bus voltage is well regulated, confirming the performance of the proposed controller against CPLs.

5 Conclusions

This article has proposed a novel adaptive technique based on p_{CH} to stabilize the DC bus voltage of a DC/DC boost converter supplied by a PEMFC and supplying both CRL and CPL. The adaptive control schemes are analyzed showing that the DC output voltage has global convergence and preserving asymptotic stability. The effectiveness of the proposed three control strategies was compared with the classic PI controller through simulations with power electronic devices and driving characteristics using MATLAB/Simulink. The theoretical claims have been systematically authenticated via digital simulations and experimental prototyping, demonstrating the practical feasibility of the method.

Finally, the proposed adaptive Hamiltonian energy control law III exhibits the best performance and is a model-based control system. It is needed to find the controlled plant parameters (such as r_L) to determine the port–Hamiltonian form. In future works, some real-time parameter estimations will be studied to improve the controlled converter.

Appendix

Figures A1 and A2 show the experimental platform, which includes a DC microgrid platform and a real PEMFC/Reformer (ME^{2}Power^{TM} FC system: 2.5 kW, 50 V), an FC step–up converter, and controller engine, using the parameters in Table A1. The electronic load Chroma^{TM} 63212E–600–840 was used to emulate the CRL and CPL. All control algorithms were digitally estimated in a MicroLabBox dSPACE DS1103 (sampling frequency = 25 kHz, synchronized with a switching frequency f_s of 25 kHz of the FC power circuit). Noted here that it is beyond the scope of this paper to discuss the sampling time delay (for example single update or double update); more details can be found in [44], [45].

Table A1: An FC boost converter parameter

Symbol	Parameter	Value
v_{FC}	Nominal FC Voltage	50 V
v_C	DC bus Voltage	120 V
L	High Frequency Inductance	250 μH
C	Output Capacitance	500 μF
S	IGBT Power Switch	VS-GT100DA120U
D	Power Diode	IXYS 61-10B
f_S	Switching Frequency	25 kHz

Figure A1: Laboratory experimental test bench of the DC microgrid platform.

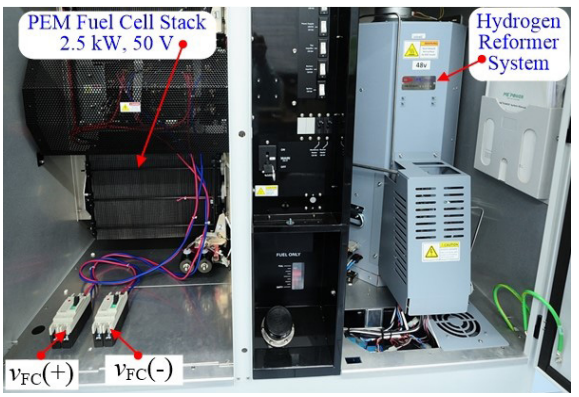

Figure A2: Laboratory experimental test bench of the 2.5 kW PEM fuel cell system.

Acknowledgement

This work was supported by the International Research Partnerships: Electrical Engineering Thai-French Research Center between Université de Lorraine (UL) and King Mongkut's University of Technology North Bangkok (KMUTNB) through the Research Program Cooperation under Grant KMUTNB−BasicR−64−17.

References

[1] F. M. Guangul and G. T. Chala, "A comparative study between the seven types of fuel cells," *Applied Science and Engineering Progress*, vol. 13, no. 3, pp. 185–194, 2020, doi: 10.14416/j.asep.2020.04.007.

[2] N. Bizon, P. Thounthong, and D. Guilbert, "Efficient operation of the hybrid power system using an optimal fueling strategy and control of the fuel cell power based on the required power tracking algorithm," *Sustainability*, vol. 12, no. 22, p. 9690, Nov. 2020.

[3] K. Sankar, G. Saravanakumar, and A. K. Jana, "Nonlinear multivariable control of an integrated PEM fuel cell system with a DC-DC boost converter," *Chemical Engineering Research and Design*, vol. 167, pp. 141–156, 2021.

[4] T. Lan and K. Strunz, "Modeling of multi-physics transients in PEM fuel cells using equivalent circuits for consistent representation of electric, pneumatic, and thermal quantities," *International Journal of Electrical Power & Energy Systems*, vol. 119, p. 105803, Jul. 2020.

[5] N. Bizon and P. Thounthong, "Energy efficiency and fuel economy of a fuel cell/renewable energy sources hybrid power system with the load-following control of the fueling regulators," *Mathematics*, vol. 8, no. 2, p. 151, Jan. 2020.

[6] W. Jiang, X. Zhang, F. Guo, J. Chen, P. Wang, and L. H. Koh, "Large-signal stability of interleave boost converter system with constant power load using sliding-mode control," *IEEE Transactions on Industrial Electronics*, vol. 67, no. 11, pp. 9450–9459, Nov. 2020.

[7] F. Naseri, E. Farjah, Z. Kazemi, E. Schaltz, T. Ghanbari, and J. Schanen, "Dynamic stabilization of DC traction systems using a supercapacitor-based active stabilizer with model predictive control," *IEEE Transactions on Transportation Electrification*, vol. 6, no. 1, pp. 228–240, Mar. 2020.

[8] P. Thounthong, P. Mungporn, S. Pierfederici, D. Guilbert, and N. Bizon, "Adaptive control of fuel cell converter based on a new Hamiltonian energy function for stabilizing the DC bus in DC microgrid applications," *Mathematics*, vol. 8, no. 11, p. 2035, 2020.

[9] A. Kwasinski and C. N. Onwuchekwa, "Dynamic behavior and stabilization of dc microgrids with instantaneous constant-power loads," *IEEE Transactions on Power Electronics*, vol. 26, no. 3, pp. 822–834, Mar. 2011.

[10] M. Cespedes, L. Xing, and J. Sun, "Constant-power load system stabilization by passive damping," *IEEE Transactions on Power Electronics*, vol. 26, no. 7, pp. 1832–1836, Jul. 2011.

[11] S. Yousefizadeh, J. D. Bendtsen, N. Vafamand, M. H. Khooban, F. Blaabjerg, and T. Dragicevic, "Tracking control for a dc microgrid feeding uncertain loads in more electric aircraft: Adaptive backstepping approach," *IEEE Transactions on Industrial Electronics*, vol. 66, no. 7, pp. 5644–5652, Jul. 2019.

[12] Q. Xu, C. Zhang, Z. Xu, P. Lin, and P. Wang, "A composite finite-time controller for decentralized power sharing and stabilization of hybrid fuel cell/supercapacitor system with constant power load," *IEEE Transactions on Industrial Electronics*, vol. 68, no. 2, pp. 1388–1400, Feb. 2021.

[13] G. C. Konstantopoulos and A. T. Alexandridis, "Generalized nonlinear stabilizing controllers for Hamiltonian-passive systems with switching devices," *IEEE Transactions on Control Systems Technology*, vol. 21, no. 4, pp. 1479–1488, Jul. 2013.

[14] R. V. Meshram, M. Bhagwat, S. Khade, S. R. Wagh, A. M. Stankovic, and N. M. Singh, "Port-controlled phasor Hamiltonian modeling and IDA-PBC control of solid-state transformer," *IEEE Transactions on Control Systems Technology*, vol. 27, no. 1, pp. 161–174, Nov. 2018.

[15] P. Mungporn, B. Yodwong, P. Thounthong, C. Ekkaravarodome, A. Bilsalam, B. Nahid-Mobarakeh, S. Pierfederici, D. Guilbert, N. Bizon, S. Khomfoi, P. Kumam, Z. Shah, and P. Burikham, "Study of Hamiltonian energy control of multiphase interleaved fuel cell boost converter," in *Research, Invention, and Innovation Congress (RI2C)*, 2019, pp. 1–6, doi: 10.1109/RI2C48728.2019.8999956.

[16] S. Pang, B. Nahid-Mobarakeh, S. Pierfederici, M. Phattanasak, Y. Huangfu, G. Luo, and F. Gao, "Interconnection and damping assignment passivity-based control applied to on-board DC–DC power converter system supplying constant power load," *IEEE Transactions on Industry Applications*, vol. 55, no. 6, pp. 6476–6485, 2019.

[17] W. He, R. Ortega, J. E. Machado, and S. H. Li, "An adaptive passivity-based controller of a buck-boost converter with a constant power load," *Asian Journal of Control*, vol. 21, no. 2, pp. 581–595, Mar. 2018.

[18] C. A. Soriano-Rangel, W. He, F. Mancilla-David, and R. Ortega, "Voltage regulation in buck–boost converters feeding an unknown constant power load: An adaptive passivity-based control," *IEEE Transactions on Control Systems Technology*, vol. 29, no. 1, pp. 395–402, Jan. 2021.

[19] P. Thounthong, P. Mungporn, S. Pierfederici, D. Guilbert, N. Takorabet, B. Nahid-Mobarakeh, Y. Hu, N. Bizon, Y. Huangfu, P. Kumam, and P. Burikham, "Robust Hamiltonian-energy control based on lyapunov function for four-phase parallel fuel cell boost converter for DC microgrid applications," *IEEE Transactions on Sustainable Energy*, vol. 12, no. 3, pp. 1500–1511, doi: 10.1109/TSTE.2021.3050783.

[20] P. Mungporn, B. Yodwong, P. Thounthong, B. Nahid-Mobarakeh, N. Takorabet, D. Guilbert, P. Kumam, N. Bizon, and C. Kaewprapha, "Model-free control of multiphase interleaved boost converter for fuel cell/reformer power generation," in *Research, Invention, and Innovation Congress (RI2C)*, 2019, pp. 1–6, doi: 10.1109/RI2C48728.2019.8999919.

[21] W. Thammasiriroj, P. Mungporn, B. Nahid-Mobarakeh, S. Pierfederici, N. Bizon, and P. Thounthong, "Comparative study of model-based control of energy/current cascade control for a multiphase interleaved fuel cell boost converter," in *International Conference on Power, Energy and Innovations (ICPEI)*, 2020, pp. 244–248, doi: 10.1109/ICPEI49860.2020.9431490.

[22] C. Gu, H. Yan, J. Yang, G. Sala, D. D. Gaetano, X. Wang, A. Galassini, M. Degano, X. Zhang, and G. Buticchi, "A multiport power conversion system for the more electric aircraft," *IEEE Transactions on Transportation Electrification*, vol. 6, no. 4, pp. 1707–1720, Dec. 2020.

[23] Y. Gao, T. Yang, S. Bozhko, P. Wheeler, and T. Dragičević, "Filter design and optimization of electromechanical actuation systems using search and surrogate algorithms for more-electric aircraft applications," *IEEE Transactions on Transportation Electrification*, vol. 6, no. 4, pp. 1434–1447, Dec. 2020.

[24] Y. Wang, S. Nuzzo, H. Zhang, W. Zhao, C. Gerada, and M. Galea, "Challenges and opportunities for wound field synchronous generators in future more electric aircraft," *IEEE Transactions on Transportation Electrification*, vol. 6, no. 4, pp. 1466–1477, Dec. 2020.

[25] M. M. Mahfouz and M. R. Iravani, "Grid-integration of battery-enabled DC fast charging station for electric vehicles," *IEEE Transactions on Energy Conversion*, vol. 35, no. 1, pp. 375–385, Mar. 2020.

[26] H. Tao, H. Hu, X. Zhu, Y. Zhou, and Z. He, "Harmonic instability analysis and suppression method based on αβ- frame impedance for trains and network interaction system," *IEEE Transactions on Energy Conversion*, vol. 34, no. 2, pp. 1124–1134, Jun. 2019.

[27] A. Tawai, K. Kitsubthawee, C. Panjapornpon, and W. Shao, "Hybrid control scheme for anaerobic digestion in a CSTR-UASB reactor system," *Applied Science and Engineering Progress*, vol. 13, no. 3, pp. 213−223, 2019, doi: 10.14416/j.asep.2020.06.004.

[28] T. Srihawan and C. Panjapornpon, "Input-output linearizing control of strong acid-base neutralization processwith fluctuation in feed pH," *Applied Science and Engineering Progress*, vol. 13, no. 4, pp. 327−335, Dec. 2019, doi: 10.14416/j.asep.2019.02.004.

[29] S. Sriprang, B. Nahid-Mobarakeh, N. Takorabet, S. Pierfederici, N. Bizon, P. Kuman, and P. Thounthong, "Permanent magnet synchronous motor dynamic modeling with state observer-based parameter estimation for AC servomotor drive application," *Applied Science and Engineering Progress*, vol. 12, no. 4, pp. 286−297, 2019, doi: 10.14416/j.asep.2019.11.001.

[30] S. Pang, B. Nahid-Mobarakeh, S. A. Hashjin, S. Pierfederici, J.-P. Martin, Y. Liu, Y. Huangfu, G. Luo, and F. Gao, "Stability improvement of cascaded power conversion systems based on Hamiltonian energy control theory," *IEEE Transactions on Industry Applications*, vol. 57, no. 1, pp. 1081–1093, 2021.

[31] P. Thounthong, P. Mungporn, D. Guilbert, N. Takorabet, S. Pierfederici, B. Nahid-Mobarakeh, Y. Hu, N. Bizon, Y. Huangfu, and P. Kumam, "Design and control of multiphase interleaved boost 516converters-based on differential flatness theory for PEM fuel cell multi-stack applications," *International Journal of Electrical Power & Energy Systems*, vol. 124, Jan. 2021, doi: 10.1109/TTE.2020.2980193.

[32] M. Komatsu, S. Terakawa, and T. Yaguchi, "Energetic-property-preserving numerical schemes for coupled natural systems," *Mathematics*, vol. 8, no. 2, p. 249, Feb. 2020.

[33] X. Lin, L. Sun, P. Ju, and H. Li, "Stochastic control for intra-region probability maximization of multi-machine power systems based on the quasi-generalized Hamiltonian theory," *Energies*, vol. 13, no. 1, p. 167, Dec. 2019.

[34] A. Liu and H. Yu, "Smooth-switching control of robot-based permanent-magnet synchronous motors via port-controlled Hamiltonian and feedback linearization," *Energies*, vol. 13, no. 21, p. 5731, Nov. 2020.

[35] T. Pham, I. Prodan, D. Genon-Catalot, and L. Lefèvre, "Economic constrained optimization for power balancing in a DC microgrid: A multi-source elevator system application", *International Journal of Electrical Power & Energy Systems*, vol. 118, p. 105753, 2020.

[36] W. Gil-González, O. Montoya, and A. Garces, "Direct power control for VSC-HVDC systems: An application of the global tracking passivity-based PI approach", *International Journal of Electrical Power & Energy Systems*, vol. 110, pp. 588–597, 2019.

[37] B. Wang, Z. Tang, W. Liu, and Q. Zhang, "A distributed cooperative control strategy of offshore wind turbine groups with input time delay," *Sustainability*, vol. 12, no. 7, p. 3032, Apr. 2020.

[38] P. Zhou, R. Yang, G. Zhang, and Y. Han, "Adaptive robust simultaneous stabilization of two dynamic positioning vessels based on a port-controlled Hamiltonian (PCH) model," *Energies*, vol. 12, no. 20, p. 3936, Oct. 2019.

[39] P. Mungporn, P. Thounthong, B. Yodwong, C. Ekkaravarodome, A. Bilsalam, S. Pierfederici, D. Guilbert, B. Nahid-Mobarakeh, N. Bizon, Z. Shah, S. Khomfoi, P. Kumam, and P. Burikham, "Modeling and control of multiphase interleaved fuel cell boost converter based on Hamiltonian control theory for transportation applications," *IEEE Transactions on Transportation Electrification*, vol. 6, no. 2, pp. 519–529, Jun. 2020.

[40] O. Montoya, W. Gil-González, and A. Garces, "Distributed energy resources integration in single-phase microgrids: An application of IDA-PBC and PI-PBC approaches," *International Journal of Electrical Power & Energy Systems*,

vol. 112, pp. 221–231, 2019.
[41] B. Wang, Z. Tang, X. Gao, W. Liu, and X. Chen, "Distributed control strategy of the leader-follower for offshore wind farms under fault conditions," *Sustainability*, vol. 11, no. 8, p. 2290, Apr. 2019.
[42] P. Thounthong, B. Nahid-Mobarakeh, S. Pierfederici, P. Mungporn, N. Bizon, and P. Kumam, "Hamiltonian control law based on lyapunov–energy function for four-phase parallel fuel cell boost converter," in *2020 International Conference on Power, Energy and Innovations (ICPEI)*, 2020, pp. 255–260, doi: 10.1109/ICPEI49860.2020.9431392.
[43] P. Thounthong, "Port–Hamiltonian formulation of adaptive PI controller for constant power load stability issue: Case study for multiphase fuel cell converters," in *2021 9th International Electrical Engineering Congress (iEECON)*, 2021, pp. 193–196, doi: 10.1109/iEECON51072.2021.9440316.
[44] L. Harnefors, R. Finger, X. Wang, H. Bai, and F. Blaabjerg, "VSC input-admittance modeling and analysis above the nyquist frequency for passivity-based stability assessment," *IEEE Transactions on Industrial Electronics*, vol. 64, no. 8, pp. 6362–6370, 2017.
[45] L. Harnefors, A. Yepes, A. Vidal, and J. Doval-Gandoy, "Passivity-based controller design of grid-connected VSCs for prevention of electrical resonance instability," *IEEE Transactions on Industrial Electronics*, vol. 62, no. 2, pp. 702–710, 2015.